

A Genderless Coupling Mechanism With Six-Degrees-of-Freedom Misalignment Capability for Modular Self-Reconfigurable Robots

Wael Saab

Robotics and Mechatronics Laboratory,
Department of Mechanical Engineering,
Virginia Tech,
Randolph Hall, Room 8,
460 Old Turner Street,
Blacksburg, VA 24061
e-mail: waelsaab@vt.edu

Pinhas Ben-Tzvi

Mem. ASME
Robotics and Mechatronics Laboratory,
Department of Mechanical Engineering,
Virginia Tech,
Goodwin Hall, Room 465,
635 Prices Fork Road,
Blacksburg, VA 24061
e-mail: bentzvi@vt.edu

This paper presents the design and integration of a genderless coupling mechanism for modular self-reconfigurable mobile robots. Modular self-reconfigurable mobile robotic systems consist of a number of self-sufficient modules that interconnect via coupling mechanisms and adopt different configurations to modify locomotion and/or manipulation capabilities. Coupling mechanisms are a critical element of these robotic systems. This paper focuses on a docking mechanism called GHEFT: a Genderless, High-strength, Efficient, Fail-safe, and high misalignment Tolerant coupling mechanism that aids self-reconfiguration. GHEFT provides a high strength and energy efficient connection using nonback drivable actuation with optimized clamping profiles that tolerate translational and angular misalignments. It also enables engagement/disengagement without gender restrictions in the presence of one-sided malfunction. The detailed design of the proposed mechanism is presented, including optimization of the clamping profile geometries. Experimental validation of misalignment tolerances and achievable clamping forces and torques is performed to demonstrate the strength, efficiency, and fail-safe capabilities of the proposed mechanism, and these results are compared to reported results of some of the existing coupling mechanisms. [DOI: 10.1115/1.4034014]

Keywords: modular robots, self-reconfiguration, docking mechanism, mobile robot

1 Introduction

Conventional industrial robots operate in controlled environments and perform specialized tasks on objects of known geometries. Engineers can ensure ideal operating conditions with near certainty. When robots operate in unstructured environments, such as outdoors, tasks, and geography may not be fully known a priori. One way in which robots may deal with these uncertainties is by adapting their structures to unstructured terrain by forming new systems and enabling new functionalities. In these scenarios, a robot with metamorphic capabilities could be of great value. These requirements have led to the study of field-deployable modular self-reconfigurable mobile robots. This class of robotic systems exhibit interconnected self-contained modules capable of sensing, processing, and actuation [1]. Modules can self-reconfigure, a process in which discrete modules dock to each other without external guidance (i.e., teleoperation) [2] through a coupling mechanism. Modules then move relative to one another to perform tasks such as locomotion and manipulation. These robots provide higher versatility, robustness, and lower production costs in comparison to a single high-capability fixed-structure robot. They may also be capable of self-repair, a process in which a damaged module is autonomously replaced in a given structure [3]. Promising applications of these robots include undersea mining, search and rescue in disaster zones, and battle field reconnaissance [4].

Over the past two decades, modular self-reconfigurable mobile robots have transitioned from simple proof-of-concept prototypes to elaborate physical systems [4]. However, they have yet to be widely adopted in field applications due to reconfiguration difficulties. One challenge hindering these efforts is the coupling mechanism's connection strength and design limitations that

exhibit low misalignment tolerant capabilities and limit relative rotation between modules in performing tasks such as locomotion and manipulation [5,6].

In this paper, a genderless, high-strength, efficient, fail-safe, and high misalignment tolerant coupling mechanism (GHEFT) [7] is presented capable of robust self-reconfiguration and self-repair. The aim of this research is to advance the development of GHEFT with thorough design and analysis to create a scalable coupling mechanism that is easily integrated into modular robots. The proposed mechanism is part of an ongoing research that is envisioned to be used on a field deployable hybrid tracked and wheeled self-reconfigurable and transformable omni-directional robot modular robot called STORM [8,9], which was inspired by the unique locomotion/manipulation functionalities demonstrated by the hybrid mechanism mobile robot [10–12].

Section 2 of this paper presents a review of existing coupling mechanisms. Section 3 defines the design requirements of a coupling mechanism. Section 4 presents the design concept of GHEFT in addition to analysis and optimizations of mechanical strength and misalignment tolerance, constant lead cam design, and coupling surface geometry. Section 5 presents dynamic simulations that verify maximum misalignment tolerances. Section 6 presents experimental validation of the analytical models and simulations on an integrated prototype and demonstrates the mechanism's strength, energy efficiency, and fail-safe capabilities. Concluding remarks and future work are discussed in Sec. 7.

2 Related Work

This section reviews several state-of-the-art coupling mechanisms with focus on genderless, fail-safe designs in order to identify necessary design requirements and current challenges.

CEBOT [13] and PolyBot [14], developed in the late 1980s and 1990s, utilize coupling mechanisms that rely on gendered male

Manuscript received December 9, 2015; final manuscript received June 6, 2016; published online September 9, 2016. Assoc. Editor: Satyandra K. Gupta.

components (cone-shaped ports and grooved pins) that insert into chamfered holes on the opposing module and latch using a spring-loaded rotating plate actuated by a shape memory alloy. This mechanism constantly consumes power to maintain a connection and provides low clamping forces, limiting the structures rigidity and robot operation time. Chamfered holes and pins offer slight misalignment tolerances in the range of a few millimeters in translations and few degrees in rotations. These gendered connections are also not fail-safe since undocking relies solely on the female coupling unit.

Existing genderless and fail-safe coupling mechanisms relying on mechanical connections include GENFA [15], SINGO [16], RoGenSiD [17], and HiGen [18]. GENFA utilizes a rotary disk that latches onto chamfered pins of an opposing module to establish a connection. Misalignment tolerance is limited by the pin's radius and chamfer angle; results indicate 1–3 mm/20 deg of translational/angular misalignment tolerance. SINGO was the first coupling mechanism to combine both genderless and fail-safe criteria by utilizing four translating jaws that slide on linear rails to engage with an opposing mechanism. Docking can be established at four orientations separated by 90 deg intervals. Its tooth profile design provided maximum misalignment tolerances of 5–35 mm and 4–22 deg. However, these represent theoretically calculated misalignment tolerances. Only pitch and yaw misalignments were experimentally validated demonstrating 4 deg of tolerance. Inspired by SINGO, the RoGenSiD utilizes four curved contour locking fingers that rotate in the roll direction to engage with an opposing module. However, to constrain roll once docked, peg-hole mechanisms were implemented resulting in a mechanism that is not strictly genderless. The resultant mechanism experimentally demonstrated misalignment tolerance in only two degrees-of-freedom (DOFs): 2–3 mm and 2.4 deg in the *X*-direction and yaw directions. Similarly, HiGen utilizes four angled docking hooks that rotate to engage an opposing module. Roll motion is constrained by teeth that could be retracted using helical guides. The docking hooks experimentally demonstrated misalignment tolerance in 4DOFs: 13.5 mm and 5 mm in the *X*- and *Y*-directions and 8–10 deg of roll and yaw directions.

A number of useful observations can be drawn from these genderless, fail-safe technologies. Excluding HiGen, all listed genderless, fail-safe coupling mechanisms ensured energy efficiency during operation by using nonback-drivable actuation. This type of actuation consumes power during the docking process; then, once a connection is established, power is no longer required to maintain a connection and accidental unlatching is prevented due to single-directional motion. It is noticeable that changes to genderless connector profile designs typically enhanced misalignment tolerance in some DOFs at the cost of reducing tolerance in others. Each mechanism utilized only one docking DOF to engage/disengage its coupling. This requires the modular robot itself, outside of the docking interface, to provide a mechanism for relative motion between coupled modules, in addition to its own locomotion requirements to relatively position and align the coupling interfaces before docking. This feature limits achievable relative rotation within a specified operating range since routed wires from the coupling mechanisms might break due to excessive rotation. This issue becomes of importance when additional wires from the docking sensors are used to provide feedback information to aid the docking process. This may also hinder the docking process if the coupling mechanism cannot be oriented to bring its respective connectors within a tolerable range.

Many other coupling mechanisms exist in the literature; however, fundamental design features limit overall performance. For example, connections relying on permanent magnets [19,20] or electromagnetic forces [21,22] do provide misalignment tolerance, rigid connections. However, tolerance is limited by magnetic field strength and typically requires a consistent power supply that may lose connection unintentionally if one module malfunctions. Connections using physical latches and pins [23–32] are typically gendered and not fail-safe—namely, a

connection can only be established by satisfying male–female gender constraints and connection disengagement is not possible in the presence of one-sided coupling mechanism malfunction.

3 Coupling Mechanism Design Requirements

Based on the review of existing coupling mechanism technologies, a coupling mechanism must efficiently dock in the presence of reasonable misalignment errors between modules. Ideally, this should be accomplished using a high-strength, fail-safe connection that does not place gendered docking constraints on the system and can provide continuous or endless rotation between the modules without damaging components.

Coupling mechanisms with a single docking/undocking DOF are suitable for modular robots relying on articulated body locomotion that incorporate additional DOFs into module designs. However, for robots that rely on tracked or wheeled locomotion that do not possess high levels of articulation, it is beneficial to incorporate an additional high-torque, relative rotational DOF within the coupling mechanism that is capable of continuous rotation. This capability would isolate the coupling mechanism from the primary modular robotic structure and reduce the burden from the robot to simultaneously locomote and align modules during the docking process. To maximize energy efficiency while docked, both DOFs (docking and relative rotation) should be actuated using nonback-drivable actuation.

Another important consideration is the versatile connection of the coupling mechanism. Modular self-reconfigurable mobile robots are usually homogenous in terms of their design in order to exploit batch fabrication. System performance should not be limited in terms of achievable configurations due to a gendered coupling mechanism (requiring male and female connectors). A genderless coupling mechanism will greatly facilitate this versatility because it allows any two modules to dock as long as their identical interfaces may be positioned within the designed misalignment tolerances.

Prior to docking, modules must relatively align themselves to ensure the coupling mechanisms can engage. However, due to unstructured terrain, propagated sensor error and control system error, both translational and angular misalignments must be anticipated by and compensated for in the mechanism design itself.

As robotic configurations scale up during the self-reconfiguration process, so do the mechanical loadings acting on the structural components of the mechanisms. Therefore, it is necessary that the design and integration of the coupling mechanism be high in strength and rigidity so as not to fail during operation.

4 Mechanical Design and Analysis of GHEFT

This section presents the mechanical design and analysis of the proposed mechanism where design requirements of a coupling mechanism discussed in Sec. 3 are integrated into the GHEFT.

Figure 1 presents the schematic diagram of the GHEFT coupling mechanism design. The mechanism is composed of three main subsystems: a stationary housing, a rotating plate, and symmetric H-grooved clamping profiles. The mechanism has 2DOFs: (1) relative rotation between the rotating plate and stationary housing and (2) symmetric translation of the clamping profiles relative to the rotating plate in a fixed slot. The stationary housing geometry may be adapted and scaled to mount it on a modular robot. The rotating plate houses the clamping DOF actuation unit. A worm gear assembly is used to implement the rotational DOF due to its high torque capability. A constant lead cam was chosen to drive the translational clamping motion due to its compact design and nonback drivability to prevent undesired unlatching. The clamping profiles act as followers when a high torque servomotor rotates a cam located behind the sliding plate. Depending on the direction of rotation, the clamping profiles either move outward or inward to meet at the center. A slip ring is incorporated within the worm gear that is capable of transmitting six signal and

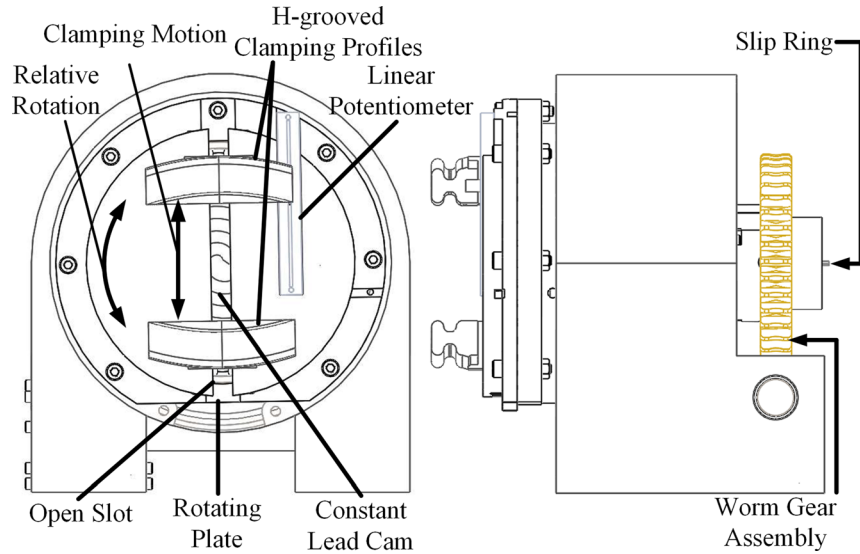


Fig. 1 Schematic diagram of GHEFT

four power circuits into the mechanism and enables continuous rotation of the sliding plate without breaking wire connections.

The clamping profiles are designed with H-grooved profiles, shown in Fig. 2(a). Each clamping profile is designed with two width (shown surfaces) and one lengthwise concave surfaces. The length wise concave surfaces have a relatively larger radius of curvature R_L . A linear potentiometer provides position feedback of the clamping profiles. To connect an opposing coupling mechanism, the profiles are driven toward the midpoint of the translational range of motion measured from the center to the edge of the sliding plate. Since clamping profiles are engaged roughly at their respective midpoints, disengagement can be achieved by sliding profiles either inward or outward depending on which surface is engaged. In the case of one-sided failure, disengagement can still be achieved by opening or closing the functional coupling mechanism without collaboration from the malfunctioning unit. Docking is performed by engaging an opposing module from either the inside or outside of its clamping profile as seen in Fig. 2(b). The clamping profiles are designed to tolerate misalignments (discussed further in Sec. 5.3) and drive the surfaces toward the docking configuration whether engaged from the inner or outer surfaces. Translation, pitch, and yaw rotation are constrained by the nested H-grooved profiles. The roll constraint requires elaboration through two case studies. Let R_C be the radius of contact with respect to the relative rotation axis of the coupling mechanism, Fig. 2(b). If $R_L = R_C$, contact friction between two concentric clamping profile surfaces is the only force constraining roll. However, the clamping profiles are designed with a large length wise radius of curvature where $R_L \gg R_C$; therefore, the two radii are never concentric and any attempt to produce roll motion will be constrained by frictional force and a surface contact moment that prevents relative roll rotation between two docked coupling mechanisms.

As opposed to previous mechanisms that utilize four genderless connectors to dock modules at four distinct localized areas about a circle, GHEFT utilizes two clamping profiles extended about two large areas of a circular parameter. This feature simplifies the design and will be shown to tolerate greater misalignments and greater force/torque loading.

4.1 Design Analysis

4.1.1 Mechanical Strength Analysis. In terms of mechanical strength, a coupling mechanism should (i) provide high clamping loading to translate and rotate modules to compensate for misalignments during docking, (ii) provide the necessary torque to

achieve relative rotation between two connected modules, and (iii) be able to tolerate loads from multiple modules connected within a robotic structure. This section analyzes the loads a coupling mechanism should be capable of withstanding and calculates the rotational DOF torque and clamping DOF forces required for robust operation.

Figure 3(a) shows a serial configuration of $N + 1$ STORM [8,9] robots with integrated GHEFT mechanisms in maximum, static gravitational loading configuration acting on the base module. Figure 3(b) shows how the stationary housing can be modified to attach onto the STORM robots. The forces and moment acting on the coupling mechanism of the first robot are calculated using the following equations:

$$T_{R,X} = \sum_{i=2}^N \sum_{j=1}^{i-1} M_i g L_j + \sum_{i=1}^N M_i g L_i / 2 \quad (1)$$

$$T_{R,Y} = \sum_{i=2}^N \sum_{j=1}^{i-1} M_i g W_j + \sum_{i=1}^N M_i g W_i / 2 \quad (2)$$

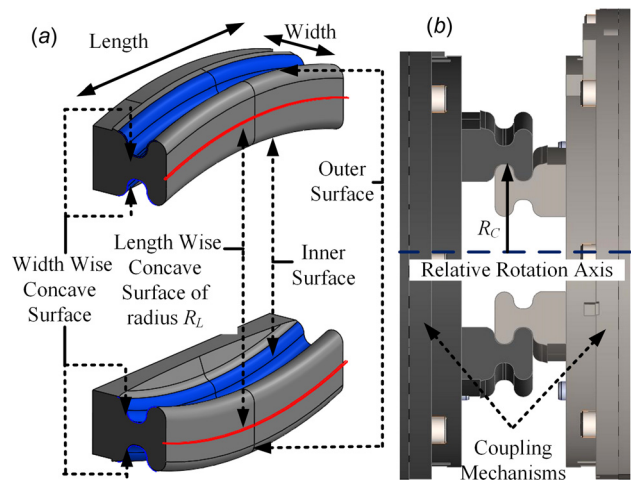


Fig. 2 (a) Isometric view of clamping profiles. (b) Side view of two docked coupling mechanisms.

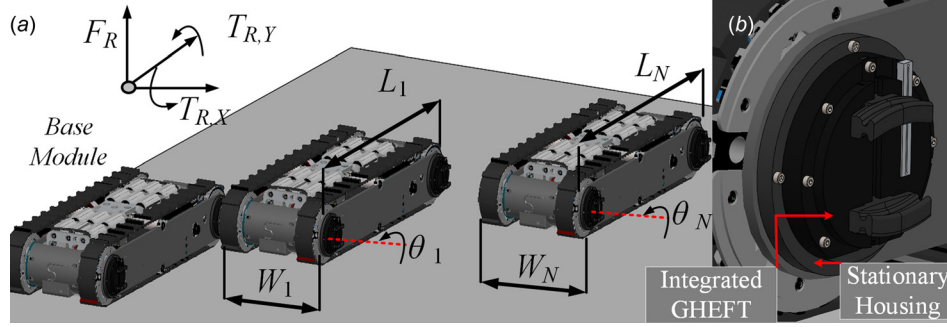


Fig. 3 (a) Serial configuration of $N + 1$ modular STORM robots with integrated GHEFT mechanisms. (b) Close-up view of integrated GHEFT mechanism.

$$F_R = \sum_{i=1}^N M_i g \quad (3)$$

where $T_{R,X}$ and $T_{R,Y}$ are the torques along X - and Y -directions; F_R is the vertical force loading; M_i , L_i , and W_i are the module i -th mass, length, and width; and g is gravitational acceleration. It is assumed the module's center of mass is at the module's geometric center. The coupling mechanism must be capable of generating $T_{R,X}$ and F_R in the relevant DOFs to generate relative rotation between two modules and to lift the mechanism during docking.

As discussed in Sec. 4, a worm-gear assembly is used to actuate the rotational DOF that overcomes $T_{R,X}$. The relative torque can be calculated based on Ref. [33]

$$T_{Rel} = T_{1,in} \frac{D_2 f \sin \lambda - \cos \phi_n \cos \lambda}{D_1 \cos \phi_n \sin \lambda + f \cos \lambda} \quad (4)$$

where $T_{1,in}$ is the motor input torque responsible for relative rotation, f is the coefficient of friction between the meshed gears, D_1 and D_2 are pitch diameters of the worm and gear, respectively, ϕ_n is the normal pressure angle, λ is the worm lead angle. The worm gear assembly scales up the magnitude of the input torque to provide a relative torque and support the load of multiple modules at a scaled down angular velocity equivalent to $\dot{\theta}_{rel} = m\dot{\theta}_{1,in}$ where m is the reduction ratio of the worm gear assembly.

As discussed in Sec. 4, a cam-follower system is used to actuate the translational DOF that overcomes F_R . Figure 4 shows a free body diagram of the cam (Body 1) split at the contact point between the cam and its followers that are engaged with an opposing coupling mechanism (Body 2). Applying the Newton-Euler formulation to Body 1 rotating at constant angular velocity yields the equations $T_{2,in} = \mu F_{N1} R + \mu F_{N2} R$ and $F_{N1} = F_{N2} = F_C$. Here, $T_{2,in}$ represents the torque input actuating the clamping DOF, R is

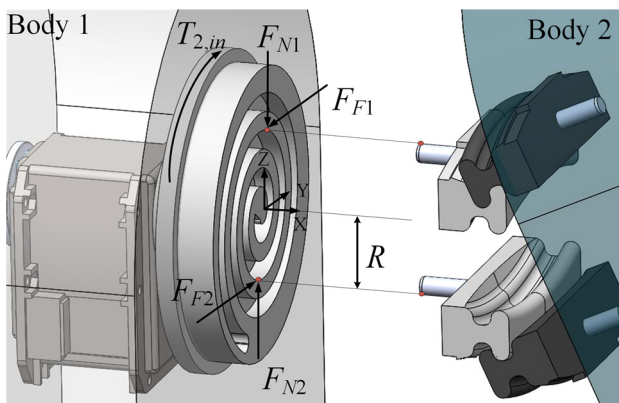


Fig. 4 Free body diagram of engaged coupling mechanisms split at the contact point between the cam and its followers

the distance between the cam center of rotation and follower, μ is the coefficient of friction, F_N are the normal contact forces, and F_C is the clamping force. Through simple substitution of these relations, the static clamping force can be computed as $F_C = T_{2,in}/2\mu R$.

It is desirable to maximize F_C in order to tolerate vertical misalignments. This may be achieved by maximizing motor torque, reducing friction between the cam and followers, and minimizing the distance between the followers during docking while still enabling fail-safe operation.

To ensure proper operations, T_{rel} and F_C must be sufficiently greater than Eqs. (1) and (3) with a sufficient factor of safety if dynamic forces are not negligible.

The following mechanical properties were used for calculations: $T_{1,in} = 3.1 \text{ N m}$, $T_{2,in} = 7.3 \text{ N m}$, $\theta_{1,in} = 8 \text{ rad/s}$, $D_1 = 0.025 \text{ m}$, $D_2 = 0.084 \text{ m}$, $m = 1/40$, $\phi_n = 14.5 \text{ deg}$, $\lambda = 4.46 \text{ deg}$, $f = 0.6$, and $\mu = 0.35$. Frictional coefficients were estimated based on surface roughness and conditions of the materials in contact [33]. With the assigned values, the mechanism can provide a static clamping force of $F_C = 297.9 \text{ N}$ occurring midway of the sliding slots ($R = 35 \text{ mm}$), an ideal location to accommodate a coupling profile from an opposing mechanism to maintain fail-safe criteria as will be demonstrated in Sec. 6, and a relative rotational torque of $T_{Rel} = 14.06 \text{ N m}$ at 0.2 rad/s .

4.1.2 Constant Lead Cam Design. With knowledge of the maximum clamping force generated by the coupling mechanism, the constant lead cam profile must be designed to tolerate the generated loads. The parametric spiral equations used to make the cam profiles are given by $x(\zeta) = a \cos \zeta$ and $y(\zeta) = a \sin \zeta$ where a is the constant cam profile design parameter that ensures an equal radial distance between two consecutive profile points and ζ determines the total length of the spiral. In particular, a minimal value of a must be determined such that the channels of the cam will not fail from loads during operation. As seen in Fig. 5, the constant lead cam grooves can be represented by extruded squares with a cylindrical pin exerting a maximum static clamping force $F_{c,max}$ that is assumed to be acting on the groove's outer most edge and distributed along the length D_p equal to the pin diameter. The shear and normal stress, τ and σ_N , acting on the groove are represented by [34]

$$\tau = \frac{6F_{c,max}}{D_p w_g^3} \left(\frac{w_g^2}{4} - y^2 \right) \quad (5)$$

$$\sigma_N = -\frac{12F_{c,max} h y}{D_p w_g^3} \quad (6)$$

where y is the distance away from the neutral axis (NA), w_g is the groove width, and h is the extruded height of the groove. Equation (5) indicates that shear stress is parabolic in shape with a maximum magnitude located at the NA ($y=0$) and zero values at

$y = \pm w_g/2$. Equation (6) indicates that maximum normal stresses are located at $y = \pm w_g/2$ with zero magnitude located at $y = 0$.

The maximum/minimum stress location due to combined loading can be computed from the vector norm of these stresses along the Y -direction equal to $y = 0$ (trivial solution), and $y = \pm 0.5\sqrt{-8h^2 + w_g^2}$ or can be located at the endpoints $y = \pm w_g/2$ [35]. At these locations, the principal stresses $\sigma_{1,2}(F_{c,max}, D_p, h, w_g)$ can be computed with a known force acting on the groove and by choosing pin diameter, profile extrusion height, and width to determine the failure mode [34].

By selecting design parameters $D_p, h = 5$ mm, $w_g = 15$ mm, chosen based on space limitations and to ensure sufficiently strong parts if profiles were 3D printed, and $F_{c,max} = 297.9$ N (calculated in Sec. 5.1), principal stresses at the critical points are computed to be $\sigma_1 = 0$ MPa and $\sigma_2 = -20$ MPa for $y = w_g/2$ and $\sigma_1 = 20$ MPa and $\sigma_2 = 0$ MPa for $y = -w_g/2$ [34]. Therefore, maximum distortion energy theory for ductile material can be applied $\sigma_1^2 - \sigma_1\sigma_2 + \sigma_2^2 \leq \sigma_Y^2$, where σ_Y represents yield strength, to prevent failure during operation. By selecting a material with a yield strength that satisfies the above inequality, the remaining design parameter can be computed where $a = D_p + w_g = 20$ mm.

4.1.3 Misalignment Analysis. This section analyzes misalignment tolerance capabilities of GHEFT and formulates an optimization of the clamping profiles to compute optimal clamping profile geometry to satisfy required tolerances based on application requirements.

Before modular robots dock, one or both modules must relatively position their docking interfaces. Once two modules are in close proximity, fine position and orientation alignments are performed with guidance from sensor feedback information (e.g., short-range IR sensors, laser positioning systems, cameras). However, due to uncertainties in sensing and/or control and the presence of debris or obstacles on rough terrain, precise alignment is not feasible. Therefore, a coupling mechanism should be capable of tolerating both translational and angular misalignments to improve the likelihood of successful docking. The 6DOF misalignments are shown in Fig. 6.

As discussed in Sec. 4, GHEFT's misalignment tolerances stem from the geometry of its H-grooved clamping profiles. As seen in Fig. 7(a) concave surfaces run along both the length and width of the clamping profiles. Each concave surface has local minima and maxima. To illustrate how the profile shape contributes to misalignment tolerance, Fig. 7(b) shows a side view of the profiles during engagement. Misalignments are tolerated if the local maxima of one profile are in contact with the concave surface of the opposing profile. If so, clamping forces generated during docking due to the misalignment will force the local maxima to slide along the concave surface and nest within their respective local minima.

Misalignment tolerance is highly dependent on the shape and dimensions of the clamping profiles. Figure 7(c) shows design parameters of the H-grooved clamping profiles in a fully open configuration: W (width), L (length), D_p (peak-peak distance), D_M

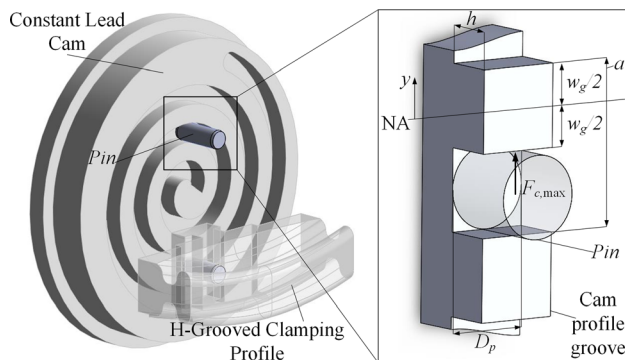


Fig. 5 Constant lead cam groove profile and parameters

(minima-minima distance). Also illustrated are the resulting angular misalignment tolerances in the roll (β), pitch (γ), and yaw (α), which are dependent on dimensions of the design parameters. Using the previous explanation on how misalignments are tolerated, relations may be formulated to calculate the clamping profile geometries based on misalignment tolerances of application requirements. Assuming modules have no angular misalignments during docking, the maximum translational tolerances in the X -, Y -, and Z -directions are equivalent to half the width, length, and distance between two local minima represented in matrix notation as $\Delta_T = [X = W/2, Y = L/2, Z = D_M/2]$. Assuming no translational misalignments, relations can be derived to express the angular misalignment tolerance as a function of design parameters using trigonometric relations represented in matrix notation as $\Delta_R = [\beta = \tan^{-1}(D_M/L), \gamma = \tan^{-1}(W/D_p), \alpha = \tan^{-1}(W/L)]$. The 6DOF misalignment tolerance nonlinear relations depend on four unknown design parameters and will be solved using optimization to compute the clamping profile geometry.

Given a set of desired maximum translational ($\Delta_{T,d}$) and rotational ($\Delta_{R,d}$) misalignment tolerances for a given application, an objective function is formulated to optimize the error e between the desired and calculated misalignment tolerances based on the relations derived above. The constrained optimization is defined as

$$\min_{W,L,D_p,D_M \in \Omega} e = \sigma_1(\Delta_{T,d} - \Delta_T)^2 + \sigma_2(\Delta_{R,d} - \Delta_R)^2$$

Subject to the set of geometric constraints

$$\Omega = \begin{cases} W_{min} \leq W \leq W_{max} \\ L_{min} \leq L \leq L_{max} \\ D_{Pmin} \leq D_p \leq D_{Pmax} \\ D_{Mmin} \leq D_M \leq D_{Mmax} \end{cases} \quad (7)$$

where σ_1 and σ_2 are scalar values to make the errors dimensionless and the constraints Ω define the clamping profile design parameters geometric boundaries based on design constraints.

The desired misalignment tolerances are chosen based on docking guidance sensor detectable range and orientation requirements. In a case scenario where the optimal detectable sensor range is contained in a rectangular volume of $5 \times 25 \times 25$ mm with orientation requirements equivalent to 40 deg in the roll and 5 deg in pitch and yaw directions, desired misalignment tolerances can be chosen: $\Delta_{T,d} = [6, 30, 30]$ mm and $\Delta_{R,d} = [45, 13, 11]$ deg

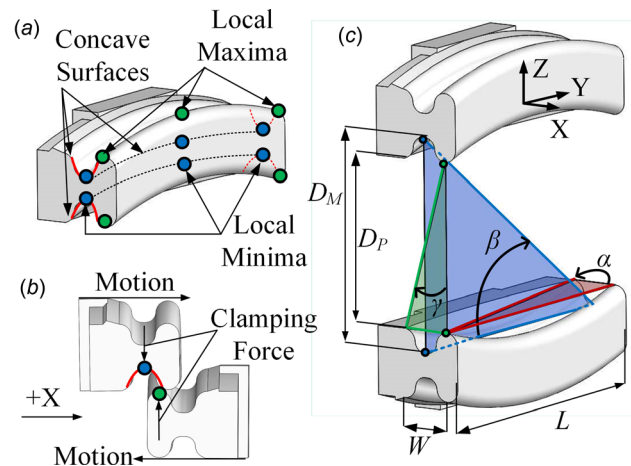


Fig. 6 6DOF misalignment tolerance experiments: (a) along X , (b) along Y , (c) along Z , (d) about Roll β , (e) about Pitch γ , (f) about Yaw α

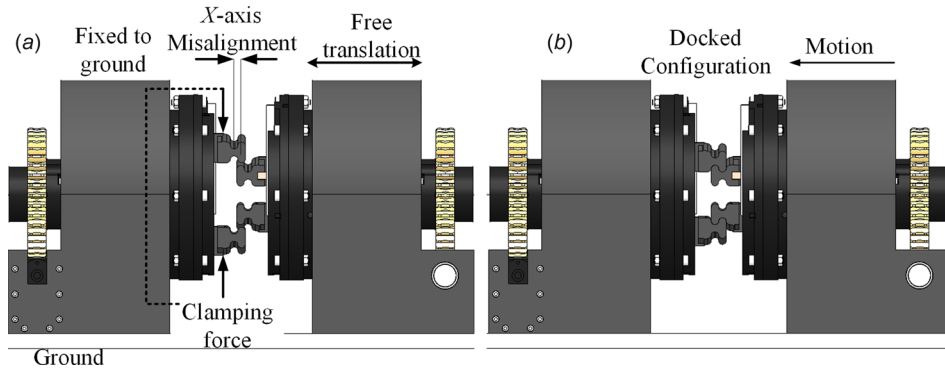


Fig. 7 (a) H-grooved clamping profiles showing peaks, local minima/maxima and concave surfaces, (b) side view of engaging clamping profiles misaligned in X-direction, (c) design parameters of clamping profiles in fully open configuration

as seen in Table 1. Using these values, Eq. (7) was solved using MATLAB nonlinear optimization toolbox constrained with lower bounds set to $[W_{\min}, L_{\min}] = [10, 40]$ mm to ensure sufficiently strong parts if profiles were 3D printed using acrylonitrile butadiene styrene (ABS) plastic and $[D_{p\min}, D_{M\min}] = [47, 50]$ mm based on minimum dimensional requirements of profile geometry in a fully open configuration. Upper limits were unconstrained. Solving Eq. (7) yields an optimal profile geometry given by: $[W = 13.9, L = 58.3, D_p = 47, D_M = 61.4]$ mm that provides computed misalignment tolerance as presented in Table 1.

5 Dynamic Simulation

In order to measure the maximum misalignments the GHEFT can tolerate, physics based simulation package, Motion Analysis, from SolidWorks [36] was used. Figure 8(a) shows the simulation setup of two opposing GHEFT mechanisms offset by a translational misalignment along the x -axis. In simulations, the mechanism on the left is fixed to the ground and is actuated by clamping forces acting on the clamping profiles (equivalent to the maximum calculated clamping forces generated by the respective servo motor). As a result, the clamping profiles close on the opposing, passive coupling mechanism that is free to move in space.

Clamping profile dimensions were chosen based on results from Sec. 5. Physical contacts between clamping profiles, external walls, and the floor were applied to the model in order to simulate physical interactions and movements of the virtual experimental setup. The maximum 6DOF misalignments were determined by increasing translational/ angular offsets incrementally in 1 mm and 1 deg increments until docking failed. Computer-aided simulations enabled precise offsets and repeatability that lead to obtaining consistent results through one trial. Figure 8(b) shows simulation results of the docked configuration where X

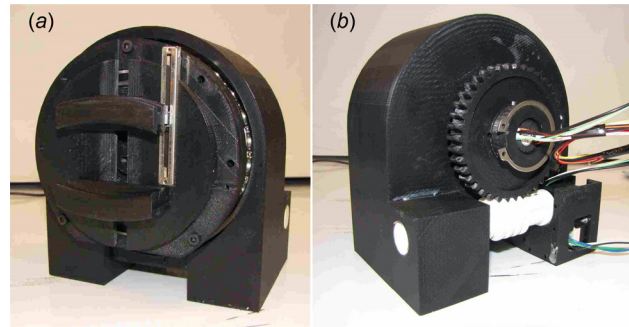


Fig. 8 (a) Dynamic simulation showing x-axis misalignment test. (b) Simulation results of the docked configuration.

misalignment was tolerated due to clamping forces that caused the passive mechanism to move left.

Table 1 summarizes results of maximum misalignment tolerance obtained from dynamic simulations. Results from dynamic simulations fall slightly below those of computed misalignment tolerances. This is expected due to frictional forces resulting from body contact that prevents successful docking within the dynamic simulation. Another source of discrepancy resulted from combined misalignments during the docking procedure. For example, Z misalignment tolerance falls significantly below its computed value due to combined pitch misalignment that accumulated as the passive module was lifted up due to gravitational forces pulling down the passive module.

6 Experimental Results

In this section, experimental studies are carried out on an integrated prototype shown in Fig. 9 to evaluate the performance of

Table 1 Desired and computed misalignment tolerance. Dynamic simulation and experimental results of misalignment tolerance and comparison to coupling mechanisms in literature. Units: translational misalignment (\pm mm), angular misalignment (\pm deg).

Misalignment	coupling mechanism	X	Y	Z	β	γ	α
Desired	GHEFT	6	30	30	45	13	11
Computed		6.9	29.1	30.7	46.4	16.5	13.4
Dyn. sim.		6	28	11	45	13	11
Experimental results		5.9 ± 0.1	24.4 ± 1.2	10.9 ± 0.1	44.5 ± 0.8	10.8 ± 0.7	10.1 ± 0.7
	GENFA [15]	1	3	3	20	20	20
	SINGO [16]	6 ^a	5–35 ^a	5–35 ^a	5.7–22 ^a	4	4
	RoGenSiD [17]	2–3	—	—	—	—	2.4
	HiGen [18]	13.5	5	—	8	—	10

^aTheoretically calculated.

— Not mentioned.

the GHEFT. Structural components were fabricated using 3D printing with ABS thermoplastic with cam and clamping profile geometries chosen based on design analysis from Sec. 5. The prototype's dimensions are $170 \times 155 \times 155$ mm and it weighs approximately 2.3 kg.

The experiments are designed to validate design analysis, and 6DOF misalignment dynamic simulations presented in Secs. 4 and 5 and demonstrate the strength, efficiency, and fail-safe capabilities of an established connection.

6.1 Experimental Setup. Experiments were conducted using a motor-actuated GHEFT module connected to a power supply and a computer. To simulate a docking target, a single-DOF analog coupling mechanism, where clamping profile motion is manually actuated by rotating an extruded shaft attached to the constant lead cam (Fig. 6), is used in conjunction with the motor-actuated GHEFT for misalignment tolerance and fail-safe experiments.

6.2 Misalignment Tolerance. Experiments were conducted to measure maximum misalignment tolerances and verify results obtained from the dynamic simulation. In these experiments, six case studies are performed where two GHEFT mechanisms are initially misaligned in each DOF. Figure 6 depicts images of the misalignment tolerance tests. The motor-actuated GHEFT is then commanded to close its clamping profiles on a passive mechanism. Misalignments are incrementally increased in 1 mm and 1 deg increments until docking failed. This procedure is repeated 20 times where the maximum translational/angular misalignment of the last recorded successful docking is documented.

Table 1 shows experimental results of misalignment tolerance measurements and provides a comparison to the highest misalignment tolerant genderless, failsafe coupling mechanisms existing in the literature. Experimental results for the GHEFT mechanism are presented as a mean and standard deviation for each misalignment DOF. Results fall slightly below those obtained from dynamic simulations (Sec. 4). This is expected since smooth surfaces of the CAD model used in simulations were not replicated in the prototype since parts were 3D printed. This resulted in high frictional forces between the rough clamping profiles surfaces that reduced experimental misalignment tolerances.

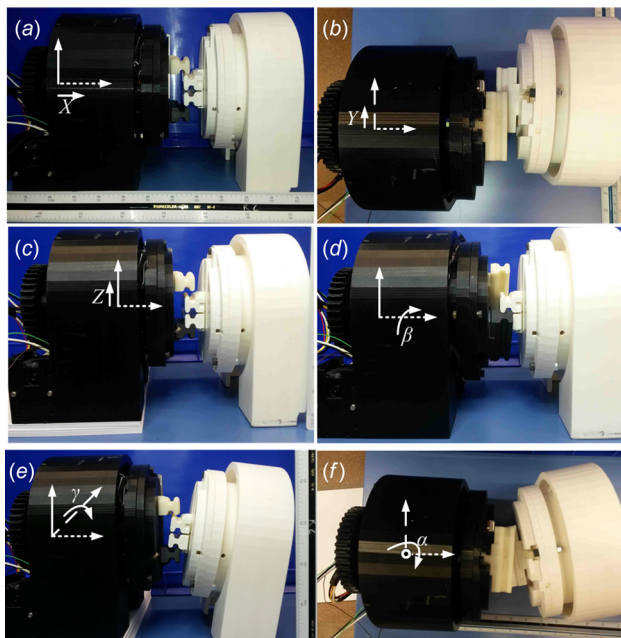


Fig. 9 Assembled prototype of GHEFT. (a) Front isometric view. (b) Back Isometric.

Results indicate that the GHEFT is capable of tolerating larger Y and β misalignments than existing mechanisms, but falls short in matching pitch and yaw angular misalignments in comparison to the GENFA coupling mechanism. The clamping profiles can however be dimensioned using previously derived relations to achieve higher tolerances in all DOFs at the tradeoff of increasing the overall size of the profiles.

The final connection between two docked mechanisms is mechanically rigid; however, in some cases, slight offset error was observed in the Y -direction ranging between ± 3 mm. This error is expected to be caused by: (1) high friction and surface roughness of the printed plastic profiles that prevents sliding and (2) zero slope of the lengthwise radius of curvature R_L at the final docked configuration that corresponds to an ineffective means of force transmission between profiles. This translational error can be overcome by quickly opening and closing the clamping profiles to induce impulsive forces that cause the profiles slide and achieve an aligned connection.

6.3 Clamping Force and Relative Torque. Experiments were performed to measure maximum clamping force and relative rotation torque the mechanism can provide to validate the model from Sec. 4. The percent actuation torque (with respect to each motor's maximum value) was varied independently while a force or moment load was applied onto the clamping profiles. Percent actuation torque was used to graphically represent input torque to the system since motors are of different specifications. Loads were incrementally increased until motors stalled, which corresponds to the maximum force or torque the mechanism can provide. Figure 10 presents experimental results of measured maximum relative torque and clamping force with a linear interpolation between data points. Maximum measured experimental results fall below computed values ($F_C = 297.9$ N and $T_{rel} = 14.06$ Nm) due to higher expected frictional coefficients resulting from variable surface conditions of the printed prototype parts. These results experimentally validate the maximum relative rotation torque and clamping force the coupling mechanism can provide and exhibit its rigidity and high strength to tolerate high loads during operation.

6.4 Energy Efficiency of Established Connection. As the power on modular self-reconfigurable mobile robots is limited, it is important that coupling mechanisms operate efficiently and consume no power once a connection between two modules is established. The GHEFT achieves this through its nonback drivable actuation; the mechanism requires no power to maintain a connection. To demonstrate the efficiency of GHEFT, various external forces were applied to the clamping profiles of the motor-actuated mechanism while performing the docking procedure.

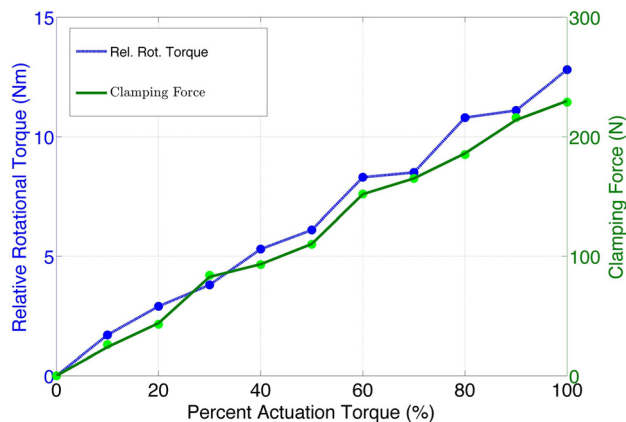


Fig. 10 Relationship between measured clamping force, relative rotational torque, and percent actuation torque

Energy was measured from a fully open clamping profile configuration until successful docking with an opposing mechanism was achieved, in a fully closed clamping profile configuration, using the relation

$$E = \sum V_i I_i \Delta t \quad (8)$$

where E represents the total energy consumed, V_i and I_i are the instantaneous voltage and current consumption, and Δt is the sampling time. Figure 11 shows the energy consumed to successfully establish and maintain a connection at various loading conditions. The data show that power consumption is monotonically increasing with applied load. Slight variations from linearity are apparent due to surface roughness of the mechanism's printed plastic parts.

A similar experiment conducted in Ref. [37] presented energy consumption of gendered coupling mechanism to establish a connection with loads varied from 0 to 15 N. In comparison to their maximum reported load, the GHEFT requires an additional 0.875 mWhrs to establish a connection. This additional energy requirement is expected to result from energy loss due to friction between the cam and followers.

6.5 Fail-Safe Capabilities. To demonstrate fail-safe capabilities, both the motor-actuated and manually actuated GHEFT mechanisms were used to test the ability to engage/disengage from a malfunctioning module similar to experiments performed in Refs. [15–18]. In this experiment, one mechanism is actuated while the other remains passive to simulate a malfunctioning module. We then test if the actuated mechanism can engage and disengage from the passive mechanism. Actuation is then switched from one mechanism to the other and we test if engagement/disengagement is successful. In these experiments, clamping profiles are engaged in the midrange of their respective open slots to provide enough room for disengagement, as discussed in Sec. 4. Following this procedure, fail-safe capabilities are successfully demonstrated with results for all four case scenarios proving that the proposed mechanism can provide modular self-reconfigurable mobile robots the ability of self-repair.

7 Conclusions and Future Work

This paper presented the design of a genderless coupling mechanism that aids the process of self-reconfiguration and self-repair for modular self-reconfigurable mobile robots. GHEFT combines critical design requirements including genderless, high-strength, energy efficiency, fail-safe, and misalignment tolerant into a

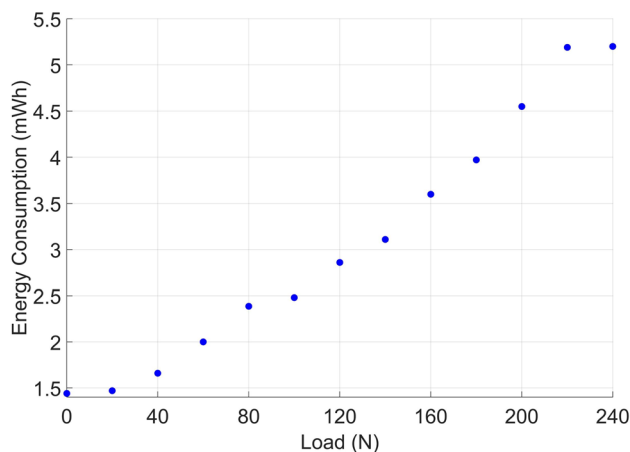


Fig. 11 Energy required to establish and maintain a connection for varied loading conditions acting on the clamping profiles

scalable mechanism. Design analysis presented justifies the selection of mechanical components and design parameters to achieve misalignment tolerance goals based on application constraints. Dynamic simulations and experimental results validate analytical models and numerical simulations, as well as demonstrate the strength, energy efficiency, and fail-safe capabilities of the mechanism.

Future work involves further analysis and optimization of clamping profile shapes that can maximize force transmission efficiency to tolerate misalignments and achieve docked configurations with minimal offset errors. The second generation GHEFT design will be modified and manufactured from metal parts to achieve a more compact, high strength mechanism with a smaller footprint. Onboard sensing technologies will be investigated and integrated to aid the docking and self-reconfiguration process of modular robots. The improved GHEFT will then be tested onboard the deployable modular robot STORM to demonstrate the docking mechanism's performance.

References

- [1] Moubarak, P., and Ben-Tzvi, P., 2012, "Modular and Reconfigurable Mobile Robotics," *Rob. Auton. Syst.*, **60**(12), pp. 1648–1663.
- [2] Groß, R., Bonani, M., Mondada, F., and Dorigo, M., 2006, "Autonomous Self-Assembly in Swarm-Bots," *IEEE Trans. Rob.*, **22**(6), pp. 1115–1130.
- [3] Murata, S., Yoshida, E., Kurokawa, H., Tomita, K., and Kokaji, S., 2001, "Self-Repairing Mechanical Systems," *Auton. Rob.*, **10**(1), pp. 7–21.
- [4] Yim, M., Zhang, Y., and Duff, D., 2002, "Modular Robots," *IEEE Spectr.*, **39**(2), pp. 30–34.
- [5] Murata, S., Kakomura, K., and Kurokawa, H., 2007, "Toward a Scalable Modular Robotic System," *IEEE Rob. Autom. Mag.*, **14**(4), pp. 56–63.
- [6] Yim, M., Shen, W.-M., Salemi, B., Rus, D., Moll, M., Lipson, H., Klavins, E., and Chirikjian, G. S., 2007, "Modular Self-Reconfigurable Robot Systems [Grand Challenges of Robotics]," *IEEE Rob. Autom. Mag.*, **14**(1), pp. 43–52.
- [7] Saab, W., and Ben-Tzvi, P., 2015, "Development of a Novel Coupling Mechanism for Modular Self-Reconfigurable Mobile Robots," *ASME Paper No. DETC2015-46659*.
- [8] Moubarak, P. M., Alvarez, E. J., and Ben-Tzvi, P., 2013, "Reconfiguring a Modular Robot Into a Humanoid Formation: A Multi-Body Dynamic Perspective on Motion Scheduling for Modules and Their Assemblies," *IEEE International Conference on Automation Science and Engineering (CASE)*, Madison, WI, Aug. 17–20, pp. 687–692.
- [9] Moubarak, P. M., and Ben-Tzvi, P., 2013, "On the Dual-Rod Slider Rocker Mechanism and Its Applications to Tristate Rigid Active Docking," *ASME J. Mech. Rob.*, **5**(1), p. 011010.
- [10] Ben-Tzvi, P., 2010, "Experimental Validation and Field Performance Metrics of a Hybrid Mobile Robot Mechanism," *J. Field Rob.*, **27**(3), pp. 250–267.
- [11] Ben-Tzvi, P., Goldenberg, A. A., and Zu, J. W., 2008, "Design and Analysis of a Hybrid Mobile Robot Mechanism With Compounded Locomotion and Manipulation Capability," *ASME J. Mech. Des.*, **130**(7), p. 072302.
- [12] Ben-Tzvi, P., Goldenberg, A. A., and Zu, J. W., 2008, "Design, Simulations and Optimization of a Tracked Mobile Robot Manipulator With Hybrid Locomotion and Manipulation Capabilities," *IEEE International Conference on Robotics and Automation (ICRA)*, Pasadena, CA, May 19–23, pp. 2307–2312.
- [13] Fukuda, T., and Kawachi, Y., 1990, "Cellular Robotic System (CEBOT) as One of the Realization of Self-Organizing Intelligent Universal Manipulator," *IEEE International Conference on Robotics and Automation, Cincinnati, OH*, pp. 662–667.
- [14] Yim, M., Duff, D. G., and Roufas, K. D., 2000, "PolyBot: A Modular Reconfigurable Robot," *IEEE International Conference on Robotics and Automation (ICRA)*, San Francisco, CA, Apr. 24–28, pp. 514–520.
- [15] Fu, G., Menciassi, A., and Dario, P., 2011, "Development of a Genderless and Fail-Safe Connection System for Autonomous Modular Robots," *IEEE International Conference on Robotics and Biomimetics (ROBIO)*, Phuket, Thailand, Dec. 7–11, pp. 877–882.
- [16] Shen, W.-M., Kovac, R., and Rubenstein, M., 2009, "SINGO: A Single-End-Operative and Genderless Connector for Self-Reconfiguration, Self-Assembly and Self-Healing," *IEEE International Conference on Robotics and Automation (ICRA)*, Kobe, Japan, May 12–17, pp. 4253–4258.
- [17] Hossain, S., Nelson, C. A., and Dasgupta, P., 2013, "RoGenSiD: A Rotary Plate Genderless Single-Sided Docking Mechanism for Modular Self-Reconfigurable Robots," *ASME Paper No. DETC2013-12938*.
- [18] Parrott, C., Dodd, T. J., and Gross, R., 2014, "HiGen: A High-Speed Genderless Mechanical Connection Mechanism With Single-Sided Disconnect for Self-Reconfigurable Modular Robots," *IEEE/RSJ International Conference on Intelligent Robots and Systems (IROS)*, Chicago, IL, Sept. 14–18, pp. 3926–3932.
- [19] Murata, S., Yoshida, E., Kamimura, A., Kurokawa, H., Tomita, K., and Kokaji, S., 2002, "M-TRAN: Self-Reconfigurable Modular Robotic System," *IEEE/ASME Trans. Mechatron.*, **7**(4), pp. 431–441.
- [20] Suh, J. W., Homans, S. B., and Yim, M., 2002, "Telecubes: Mechanical design of a Module for Self-Reconfigurable Robotics," *IEEE International Conference*

- on Robotics and Automation (ICRA), Washington, DC, May 11–15, pp. 4095–4101.
- [21] Goldstein, S. C., Campbell, J. D., and Mowry, T. C., 2005, “Programmable Matter,” *Computer*, **38**(6), pp. 99–101.
- [22] Zykov, V., Mytilinaios, E., Adams, B., and Lipson, H., 2005, “Robotics: Self-Reproducing Machines,” *Nature*, **435**(7039), pp. 163–164.
- [23] Moubarak, P. M., Ben-Tzvi, P., Ma, Z., and Alvarez, E. J., 2013, “An Active Coupling Mechanism With Three Modes of Operation for Modular Mobile Robotics,” IEEE International Conference on Robotics and Automation (ICRA), Karlsruhe, Germany, May 6–10, pp. 5489–5494.
- [24] Yim, M., Zhang, Y., Roufas, K., Duff, D., and Eldershaw, C., 2002, “Connecting and Disconnecting for Chain Self-Reconfiguration With PolyBot,” *IEEE/ASME Trans. Mechatron.*, **7**(4), pp. 442–451.
- [25] Castano, A., Behar, A., and Will, P. M., 2002, “The Conro Modules for Reconfigurable Robots,” *IEEE/ASME Trans. Mechatron.*, **7**(4), pp. 403–409.
- [26] Shen, W.-M., and Will, P., 2001, “Docking in Self-Reconfigurable Robots,” *IEEE/RSJ International Conference on Intelligent Robots and Systems*, Maui, HI, Oct. 29–Nov. 3, pp. 1049–1054.
- [27] Zykov, V., and Lipson, H., 2006, “Fluidic Stochastic Modular Robotics: Revisiting the System Design,” *Robotics Science and Systems Workshop on Self-Reconfigurable Modular Robots*, Philadelphia, PA.
- [28] Jorgensen, M. W., Ostergaard, E. H., and Lund, H. H., 2004, “Modular ATRON: Modules for a Self-Reconfigurable Robot,” IEEE/RSJ International Conference on Intelligent Robots and Systems (IROS), Sendai, Japan, Sept. 28–Oct. 2, pp. 2068–2073.
- [29] Ünsal, C., Kiliççöte, H., and Khosla, P. K., 2001, “A Modular Self-Reconfigurable Bipartite Robotic System: Implementation and Motion Planning,” *Auton. Rob.*, **10**(1), pp. 23–40.
- [30] Mondada, F., Bonani, M., Magnenat, S., Guignard, A., Floreano, D., Groen, F., Amato, N., Bonari, A., Yoshida, E., and Kröse, B., 2004, “Physical Connections and Cooperation in Swarm Robotics,” 8th Conference on Intelligent Autonomous Systems (IAS8), Amsterdam, The Netherlands, Mar. 10–14, pp. 53–60.
- [31] Murata, S., Yoshida, E., Kurokawa, H., Tomita, K., and Kokaji, S., 2001, “Self-Repairing Mechanical Systems,” *Autonomous Robots*, **10**(1), pp. 7–21.
- [32] Moubarak, P. M., and Ben-Tzvi, P., 2014, “A Tristate Rigid Reversible and Non-Back-Drivable Active Docking Mechanism for Modular Robotics,” *IEEE/ASME Trans. Mechatron.*, **19**(3), pp. 840–851.
- [33] Shigley, J. E., 2011, *Shigley’s Mechanical Engineering Design*, Tata McGraw-Hill Education, New York.
- [34] Hibbeler, R. C., 2008, *Mechanics of Materials*, Pearson Prentice Hall, Upper Saddle River, NJ.
- [35] Cartan, H., and Cartan, H. P., 1971, *Differential Calculus*, Hermann, Paris.
- [36] Dassault Systèmes, 2013, “SolidWorks: Motion Analysis,” Waltham, MA.
- [37] Delrobaei, M., and McIsaac, K. A., 2009, “Connection Mechanism for Autonomous Self-Assembly in Mobile Robots,” *IEEE Trans. Rob.*, **25**(6), pp. 1413–1419.